Check for updates

Capillary detachment of a microparticle from a liquid–liquid interface†

Sazzadul A. Rahat, [ID] [a] Krishnaroop Chaudhuri [ID] [b] and Jonathan T. Pham [ID] *[ab]

The attachment and detachment of microparticles at a liquid–liquid interface are common in many material systems, from Pickering emulsions and colloidal assemblies to capillary suspensions. Properties of these systems rely on how the particles interact with the liquid–liquid interface, including the detachment process. In this study, we simultaneously measure the capillary detachment force of a microparticle from a liquid–liquid interface and visualize the shape of the meniscus by combining colloidal probe microscopy and confocal microscopy. The capillary behavior is studied on both untreated (hydrophilic) and fluorinated (hydrophobic) glass microparticles. The measured force data show good agreement with theoretical calculations based on the extracted geometric parameters from confocal images of the capillary bridge. It is also evident that contact line pinning is an important aspect of detachment for both untreated and fluorinated particles.

Introduction

Microscale particles at liquid–liquid interfaces are found in a host of applications, for example in Pickering emulsions,[1–3] interfacial stabilizers,[4–7] colloidal particle assemblies,[8–15] and capillary suspensions.[16–18] For Pickering emulsions, particles are used to stabilize two immiscible fluids, like oil and water.[1] The stability of such emulsions relies on how the particles interact with the liquid–liquid interface, which can be important for applications in foods,[19–21] personal care products,[22,23] and oil recovery.[24,25] Moreover, harnessing particles at liquid interfaces enables hierarchical design of functional materials, as well as organisms in nature.[26–29] In the example of capillary suspensions, which are comprised of microparticles mixed with a major liquid and a minor liquid, capillary bridges of the minor liquid hold particles together to form a paste-like colloidal gel.[16,18] The rheological properties of such materials are associated with microscopic capillary bridges that hold the particles together at these liquid–liquid interfaces.[30–32] Additionally, microscale liquid–liquid and liquid–solid interfaces are important for wetting and adhesion of soft, multi-phase materials.[33–35] Given the importance of microscale capillarity, it would be beneficial to understand microparticle capillary bridges and the associated forces at a liquid–liquid interface.

The capillary force on a single particle is related to geometric parameters, like the contact angle and the position of the contact line, as well as material properties, like the interfacial tension.[36,37] Although efforts in understanding the wetting and contact angles of particles at fluid interfaces have been of great interest, there are limited capabilities in visualization of a capillary bridge on a moving particle.[38–40] For example, freeze casting and gel casting have been demonstrated as a useful method for determining contact angles of particles at high resolution.[41,42] However, the particles are usually frozen in place so they can be imaged (*e.g.* by electron microscopy); therefore, this method is most useful for static cases. Colloidal probe microscopy can be employed to measure forces on a moving particle, although traditionally this method cannot image the contact.[43–53] To address this issue, colloidal probe microscopy can be combined with simultaneous interferometry,[54–56] total internal reflection fluorescence microscopy,[57–59] fluorescence lifetime imaging microscopy[60–62] or confocal microscopy.[63–69] Schellenberger *et al.* employed colloidal probe and confocal microscopy to visualize a microparticle detaching from a gly-cerol–air interface, but did not consider liquid–liquid interfaces, nor the effect of particle surface energy.[68] On the other hand, Anachkov *et al.* employed colloidal probe microscopy to measure the detachment of a particle from a liquid–liquid interface and with different particle surface energies.[70] Force-displacement curves showed a reasonable fit to their theoretical model, but required some assumptions on contact angles since there was no image validation.

The primary goal here is to experimentally investigate how a microparticle comes into contact and detaches from a liquid–liquid interface. Using a combination of confocal microscopy

[a] Mechanical and Materials Engineering, University of Cincinnati, Cincinnati, OH 45221, USA. E-mail: Jonathan.Pham@uc.edu

[b] Chemical and Environmental Engineering, University of Cincinnati, Cincinnati, OH 45221, USA

† Electronic supplementary information (ESI) available. See DOI: https://doi.org/10.1039/d3sm00470h

and colloidal probe microscopy, we simultaneously measure the force during retraction and detachment while imaging the meniscus. Specifically, we use unmodified and fluorinated glass microparticles to study a glycerol–silicone oil interface. Confocal microscopy allows us to validate the force–distance data as well as image the geometric parameters of the liquid bridge. We show that the force data is reasonably fit to theoretical calculations based on the contact angles and interfacial tensions. Our results demonstrate that contact line pinning is an important aspect of the retraction process for both unmodified and fluorinated glass particles. In addition, we show that the forces during retraction are smaller for fluorinated particles, compared to an unmodified glass microsphere.

Results and discussion

For our experiments, glycerol and silicone oil are chosen to serve as the liquid–liquid interface, since they are immiscible, do not readily evaporate, and spread well. To prepare our samples, glycerol is spin-coated onto a glass bottom Petri dish to a thickness of $\sim$3.5 μm. Afterward, $\sim$30–50 μL of silicone oil is deposited, which spreads and creates a glycerol–oil interface. To make sure that oil does not form any contact line forces along the cantilever, both the particle and cantilever should be submerged in oil. Therefore, we ensure that the oil layer thickness is larger than 15 μm (max retracting distance). To clearly visualize the interface in our confocal microscope, 5(6)-carboxyfluorescein dye is mixed with glycerol. For our colloidal probe, we use glass microspheres (radius, R = 5.7–7.3 μm), which are attached to stiff, tipless cantilevers. In addition, we investigate the effect of surface energy by using both unmodified (*i.e.* hydrophilic) and fluorosilane-modified (*i.e.* hydrophobic) colloidal probes.

In a typical experiment, the particle is approached towards the glycerol surface at a speed of 2 μm s^{-1}, while being imaged by a confocal microscope from the bottom (Fig. 1a). The cantilever is configured roughly parallel to the glycerol–oil interface, as in a standard colloidal probe setup. Note that the entire cantilever is submerged, such that no capillary forces arise from the surrounding oil. Upon contact with the glycerol film, a meniscus forms that leads to a capillary force on the microsphere, normal to the liquid–liquid interface. After a 5-second pause, the particle is withdrawn at a speed of 0.3 μm s^{-1}. During this retraction step, the meniscus undergoes a continuous shape change until the liquid bridge disengages from the microsphere.

To fully describe the capillary behavior, it is useful to know the geometric parameters of the meniscus. With the ability to visualize the capillary bridge, we measure the relevant angles, allowing us to compare our experimental data to an established force equation. The capillary force exerted on the microsphere can be given by the following formula,[36,37]

$$F = 2\pi\gamma R \sin\beta \sin\alpha = 2\pi\gamma R \sin\beta \sin(\theta + \beta) \quad (1)$$

where R is the radius of the microsphere, γ is the interfacial tension acting along the three-phase contact line, β is an angle that indicates the position of the three-phase contact line on
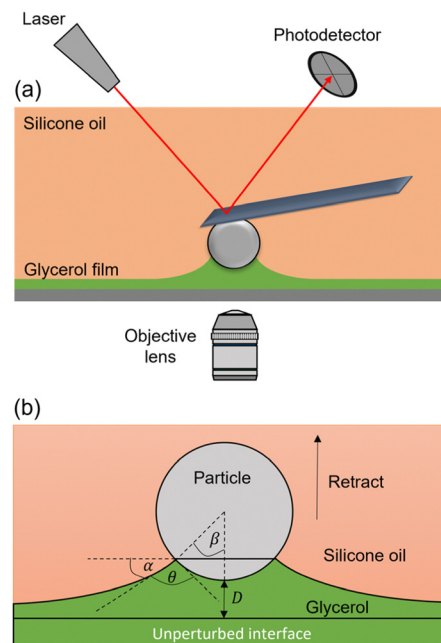

Fig. 1 (a) Colloidal probe experimental setup for a liquid–liquid interface, mounted over a confocal microscope. (b) Schematic image of the experiment showing relevant geometric parameters. θ is the contact angle, β is the position of three-phase contact line, α is the angle between the interface and the horizontal, and D is distance from the unperturbed interface.

the particle, θ is the contact angle, and α is the angle of the liquid–liquid interface relative to the horizontal (Fig. 1b). In addition, D is the distance of the microparticle relative to the unperturbed surface and the relation between angles is $\alpha = 180° - \beta - \theta$.[36,37,68] During the detachment process, two different phenomena for a three-phase contact line may arise: Either the contact line remains stationary until a threshold force is exceeded (*i.e.* the contact line is pinned)[15,68] or it slides continuously over the particle (*i.e.* the contact line is not pinned).[70,71]

For the case of a pinned contact line, β remains constant until a particular capillary force is overcome, while θ changes throughout the entire retraction process. Conversely, in the case of a fully sliding contact line, θ remains constant while the contact line moves with a varying β. The maximum capillary force is reached when $\beta_{\max} = (\pi - \theta)/2$; substituting this to eqn (1) leads to the following expression for maximum capillary force,[36,37,68]

$$F_{\max} = 2\pi\gamma R \cos^2\left(\frac{\theta_{\mathrm{r}}}{2}\right) \quad (2)$$

We first start by describing our results for an unmodified (hydrophilic) glass microparticle (R = 7.3 μm) at a glycerol–oil interface. In Fig. 2, we show a representative set of confocal images (Fig. 2a and Movie S1, ESI†) with the corresponding force–time (Fig. 2b) and force–distance (Fig. 2c) curves. For most of the approach step, the particle is not yet in contact with the glycerol film (t = 0.6 s and 5.5 s); hence, no force is detected (black triangles in Fig. 2b(i, ii) and c(i, ii)). An oscillation in the
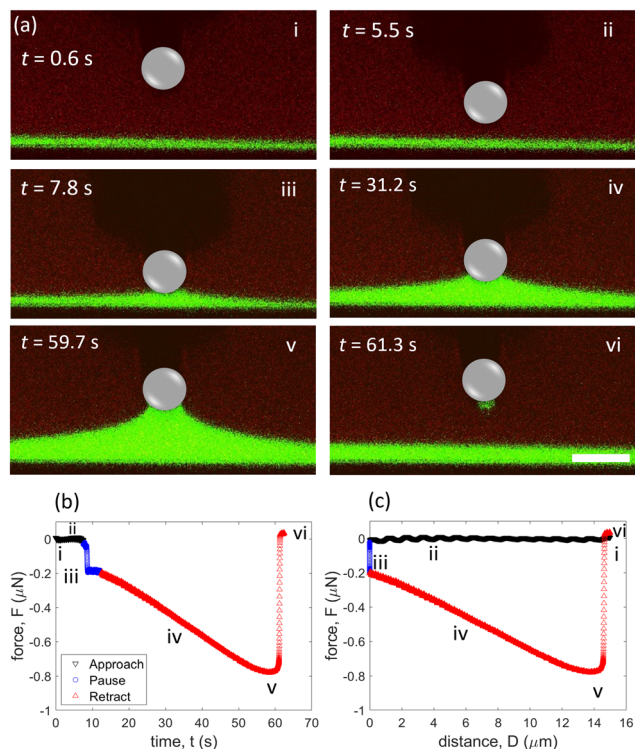
Fig. 2 Measuring capillary force and contact geometry with an unmodified (hydrophilic) glass microparticle at a glycerol–oil interface (scale: 20 μm). (a) Cross-sectional images are obtained using confocal microscopy. (i) and (ii) Approach step, position of the particle at t = 0.6 s and at t = 5.5 s, (iii) particle touches the interface, (iv) retracting the particle from the interface, (v) position of the particle at maximum capillary force, (vi) meniscus detachment. The corresponding (b) force–time curve and (c) force–distance curve, showing the different labeled points. The particle size is R = 7.3 μm.

force during the zero-contact region can be observed, which likely arises from optical inference but should not affect contact forces.[72,73] The confocal images confirm that the interface is flat (Fig. 2a(i) and (ii)) without contact. At the end of the approach ($t \approx 7.5$ s), a sudden jump in force of ~ 0.2 nN is observed (Fig. 2b(iii) and c(iii)). The confocal images indicate that the sudden jump in force is attributed to the formation of a meniscus around the particle (Fig. 2a(iii)). The capillary force of a meniscus is associated with two mechanisms.[74–78] The first is the interfacial tension of the glycerol–oil interface that engages directly around the periphery of the meniscus and pulls down on the particle. The second is related to the capillary pressure due to the curvature.

Due to the wettability, glycerol flows from the far field of film and tends to accumulate around the particle. Consequently, the local thickness of glycerol film increases during contact, as indicated by confocal imaging (Fig. 2a(iii)). Previously, it was demonstrated using a glycerol–air interface that a plateau in force (which suggests equilibrium) can be achieved by holding the particle stationary for ~ 60 minutes before retracting. However, for such long dwell times, we find that it is not possible to detach the particle from the glycerol–oil interface at the maximum moving limit of our atomic force microscope. Hence, the particle

is kept stationary for 5 s before retraction. Note that since we are able to measure the geometric parameters, we are not necessarily aiming to reach an equilibrium plateau in force. Hence, one of the unique aspects of our work is validating capillary force equations with measured contact line angles in real-time. During the retraction step, the meniscus extends steadily in the normal direction and reaches a maximum capillary force of ~ 0.8 μN at $D \approx 14$ μm and $t \approx 59.7$ s (Fig. 2a(v), b(v) and c(v)). After this point, the capillary force begins to decrease and the meniscus ruptures around $D \approx 14.5$ μm (Fig. 2a(vi), b(vi) and b(vi)). After breaking of the capillary bridge, the glycerol film returns to being flat and the force returns to zero. To confirm repeatability, we measured the capillary force three times after cleaning the colloidal probe with acetone and allowing sufficient time for drying (Fig. S1a, ESI†).

For the fluorinated (hydrophobic) case, a modified glass microsphere of similar size (R = 5.7 μm) is used as the colloidal probe. In a similar form to Fig. 2, representative confocal images are presented (Fig. 3a and Movie S2, ESI†) with the corresponding force–time (Fig. 3b) and force–distance (Fig. 3c) curves. The same experimental measurement conditions are maintained to test the fluorinated probes in comparison to the unmodified glass probes and also measured three times (Fig. S1b, ESI†). Like the unmodified glass experiments, the particle does not interact with the glycerol film for most of the approaching period (Fig. 3a(i) and (ii)). When the particle encounters the glycerol–oil interface, no jump in force is detected (Fig. 3b(iii) and c(iii)). This contrasts with the attractive jump in force observed in the unmodified, hydrophilic case at $t \approx 7.5$ s (Fig. 2b(iii) and c(iii)). With the unmodified microparticle, a clear meniscus forms when it contacts the interface (Fig. 2a(iii)). Conversely, the formation of a meniscus is hardly visible in confocal imaging during the initial contact and stationary period for the fluorinated, hydrophobic case (Fig. 3a(iii)).

When the particle is retracted from the interface, an increase in capillary force is measured (Fig. 3b(iv) and c(iv)), demonstrating that an adhesive contact is made between the particle and the glycerol–oil interface. In confocal images, it is clear that the glycerol film is pulled up with the retracting particle, which is consistent with the increase in the measured capillary force (Fig. 3a(iv), b(iv) and c(iv)). The meniscus extends until a force of ~ 0.36 μN is reached at $D \approx 7.7$ μm and $t \approx 38.8$ s (Fig. 3a(v), b(v) and c(v)). With continued extension, the particle detaches at $D \approx 8.1$ μm and $t \approx 39.5$ s (Fig. 3a(vi), b(vi) and c3(vi)). Both the maximum force and the detachment distance are less than half of that of the unmodified case, illustrating that the fluorinated surface interaction leads to a reduction in maximum capillary force (Fig. 2c(v) *vs.* 3c(v)).

Oftentimes, it is necessary to make assumptions about the contact line behavior to compare experimental results to capillary force equations. For example, it is sometimes assumed that the contact line slides along the particle when it is being retracted.[36,70,71] However, in our particular case, confocal images suggest that the contact line is pinned for both the unmodified and the fluorinated particles until the meniscus is on the verge of rupture. To gain more insight into the contact line motion, we plot the contact angle (θ), the position of the
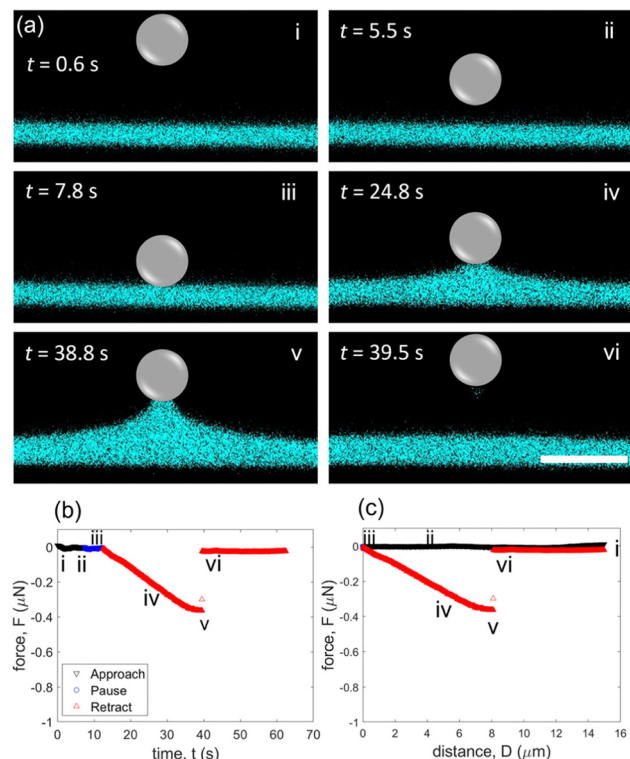
Fig. 3 Measuring capillary force and contact geometry with a fluorinated (hydrophobic) glass microparticle at a glycerol–oil interface (scale: 20 µm). (a) Cross-sectional images are obtained using confocal microscopy. (i) and (ii) Approach step, position of the particle at $t = 0.6$ s and at $t = 5.5$ s, (iii) particle touches the interface, (iv) retracting the particle from the interface, (v) position of the particle at maximum capillary force, (vi) meniscus detachment. The corresponding (b) force–time curve and (c) force–distance curve, showing the different labeled points. The particle size is $R = 5.7$ µm.

Fig. 4 Distribution of θ, β and α with respect to time for (a) unmodified (hydrophilic) and (b) fluorinated (hydrophobic) case. Angles are measured for three sets of experiments and error bars represent 10% error.

three-phase contact line (β), and position of interface relative to the horizontal (α) as a function of time for both cases (Fig. 4). For the unmodified glass sphere, θ remains relatively constant when the particle is stationary between $t \approx 7.5$ s and $t \approx 12.5$ s. However, when the particle starts to retract at $t \approx 12.5$ s, there is a clear decrease in θ. Over the course of retraction, θ decreases from $\sim 132°$ to $74°$ and the value of α increases from $\sim 10°$ to $59°$. On the other hand, β remains constant ($\sim 45°$) for most of the retraction period, confirming that the contact line is pinned on the timescale of the experiment. Therefore, it can be concluded that the capillary force is associated with changes in θ and α instead of a changing β, which would be the case if the contact line is fully sliding. Shortly before detachment, β starts to decrease, illustrating that the contact line starts sliding before detaching.

Recently, it was reported that contact line pinning is associated with the roughness of the particle, and a threshold RMS roughness for contact line pinning is ~ 17 nm.[79] To gain insight into the pinning mechanism that is observed in our experiments, we measure the roughness of the glass microspheres used as colloidal probes. These measurements indicate that the RMS roughness is below ~ 10 nm. However, the maximum peak-to-valley values
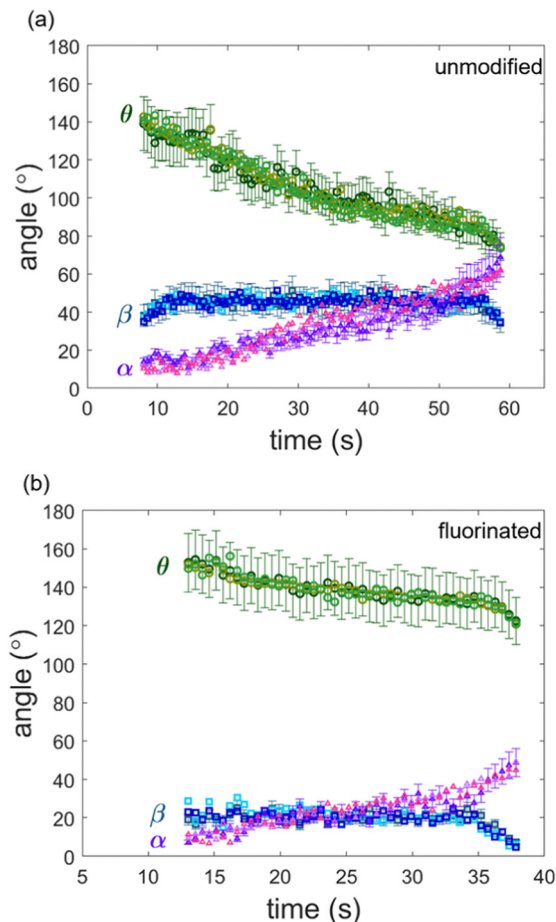
range between ~ 30–100 nm (Fig. S2, ESI†). Hence, it is likely that the contact line pinning observed during capillary force measurement can be attributed to these peaks on the microsphere. Moreover, pinning might still occur at RMS roughness of under ~ 10 nm, as opposed to true smooth surfaces with a roughness under ~ 1 nm. Hence, our results suggest that pinning, likely due to roughness, governs most of the force–distance curve regardless of surface treatment.

To compare our results to the maximum force calculated from eqn (2), it is necessary use know the receding contact angle (θ_r). We considered the contact angle measured immediately before sliding occurs as the receding contact angle. From Fig. 4a, we see that β starts declining at $t \approx 55.5$ s, which corresponds to $\theta_r \approx 85°$. In addition, it is also necessary to know the interfacial tension of the glycerol–oil interface; this is measured to be 32.5 ± 0.5 mN m^{-1} (Fig. S3, ESI†), which is consistent with literature.[80] Substituting these values into eqn (2) predicts the maximum capillary force to be $F_{\text{max,unmodified}} = 0.81$ µN, which is close to the measured maximum capillary force ~ 0.8 µN.

For the fluorinated case, contact line pinning is also observed. The position of the contact line (β) remains relatively constant ($\sim 20°$) over most of the retraction, confirming a
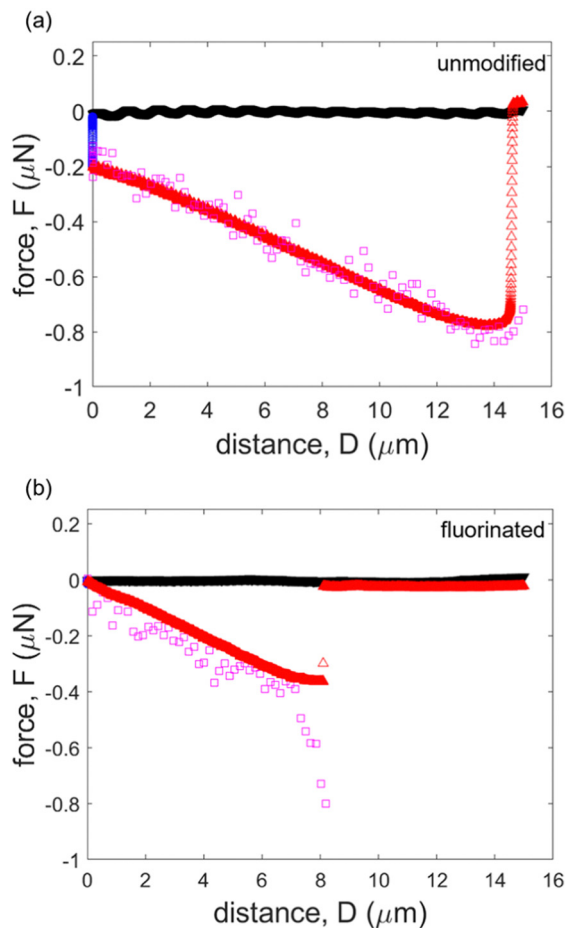
Fig. 5 Comparison of theoretically calculated force and experimentally measured force. (a) Unmodified (hydrophilic) case, (b) fluorinated (hydrophobic) case.

pinned contact line. The contact angle (θ) decreases from $\sim 151°$ at $t \approx 12.5$ s to $\sim 120°$ at $t \approx 37.5$ s and α increases from $\sim 10°$ to $50°$. This decrease in θ is much less drastic than for the unmodified case. Here we find $\theta_r \approx 83°$. Hence, eqn (2) predicts $F_{\text{max,fluorinated}} = 0.65$ μN. This is not very close to the measured value of ~ 0.36 μN. Since the capillary bridge is less pronounced for the fluorinated case, measuring contact angles accurately is challenging, which may be one reason for this discrepancy in $F_{\text{max,fluorinated}}$.

To gain more insight beyond the maximum force (eqn (2)), we also compare our results to eqn (1) throughout the entire detachment process. These calculations are made using the measured values for θ, β and γ throughout the experiment, and overlaid on experimental force–distance curves for both unmodified and fluorinated cases. As illustrated in Fig. 5(a), the calculated forces match the experimentally measured values rather well for the unmodified glass particle, confirming the validity of eqn (1). Note that within our short experimental time frame (~ 60 s), the angles at the contact line are still able to describe the capillary force, and a long equilibrium time does not appear to be necessary. However, it is possible that much longer experiment times will lead to different results associated

with glycerol flow. For the fluorinated case, the capillary force predictions follow the measured values for the majority of the experiment. However, the predicted capillary force does not fit the measured data near the detachment point, where the glycerol meniscus is on the verge of breaking (Fig. 5b); this is consistent with our discussion about the maximum capillary force above, F_{max}. Discrepancies in this calculated force might be explained by an unstable bridge in the contact region. Upon reaching the maximum force near the detachment distance, the bridge can become unstable, leading to a rapid detachment. This fast separation event is likely not fully captured by our imaging due to limitations in our frame rate (~ 2 images per second). This may affect the validity of our contact angle measurements by confocal microscopy in the fast detachment region; however, the force–distance data from AFM is not affected since the sampling rate is sufficiently fast. The lower surface energy of the fluorinated particle seems to accelerate the detachment process. This is supported by the measured force data (Fig. 5(b)), which indicates a very rapid detachment of the particle. In the unmodified case, there are many data points between the maximum force and the actual detachment point (when the force goes back to zero). In the fluorinated case, however, there are effectively only one or two data points that are captured. As a result, it is difficult to image the changes in angles.

Conclusions

We experimentally investigate how a microparticle attaches and detaches from liquid–liquid interface. We measure the detachment force while simultaneously visualizing the liquid meniscus by combining confocal microscopy with colloidal probe microscopy. By using both unmodified and fluorinated glass microparticles, our results show that lower surface energy particles have a smaller capillary force. Confocal images demonstrate that the contact line is evidently pinned for both unmodified and fluorinated particles until the liquid bridge is on the verge of detachment. Hence, changes in capillary force are related to a change in contact angle of a pinned contact line. We validate an established force equation by using measured geometric parameters and interfacial tension. However, our theoretical calculations exhibit discrepancies for the fluorinated particle near the detachment point, likely because of a rapid detachment event that is not easily captured in confocal images.

Experimental

Preparation of glycerol–oil interface

Glycerol fluorescence. We used 5(6)-carboxyfluorescein (Sigma-Aldrich) dye to visualize the glycerol film in the confocal microscope. 5(6)-Carboxyfluorescein was first dissolved in acetone (VWR) with a concentration of ~ 8.5 mg g^{-1} of acetone. Later, the dye solution was mixed with glycerol using a vortex mixer with a concentration of ~ 200 μg g^{-1} of glycerol. The dyed glycerol was kept in a desiccator for ~ 2 hours to remove residual acetone.

Silicone oil fluorescence. Nile red (ThermoFisher) dye was dissolved in acetone (VWR) with a concentration of ∼2.5 mg g^{-1} of acetone. The resulting solution was blended with silicone oil (polydimethylsiloxane, trimethylsiloxy terminated, 5 cst, Gelest) with a concentration of ∼75 μg g^{-1} of silicone oil. The dyed silicone oil was left in a desiccator for ∼2 hours to eliminate any remaining acetone in the solution.

Glycerol film preparation. The dyed glycerol was spin-coated on a glass-bottom Petri dish (Matsunami, VWR, Size no. 0) at 4500 rpm for 120 seconds. Thus, a glycerol film of approximately 3.5 μm in thickness was obtained. The glass-bottom Petri dish was cleaned in a UV-ozone chamber (Jelight) for 15 minutes prior to spin-coating. Following the spin-coating of glycerol, ∼30–50 μL of dyed silicone oil was deposited onto the surface of the glycerol film. As the surface tension of silicone oil is low, it spreads over the glycerol film and a glycerol–silicone oil interface was formed. Subsequently, the sample was rested for ∼15 minutes to allow the interface to equilibrate.

Characterization

Colloidal probe microscopy. We used a JPK Nanowizard 4a atomic force microscope to quantify the capillary force exerted on a microparticle. Additionally, we employed two distinct particle types – unmodified glass particles and fluorinated, surface-treated particles. Polydisperse soda lime glass microspheres (Cospheric) of ∼5.7 μm and 7.3 μm radius were glued to tipless silicon cantilevers (AppNano, SPM Probe ACL, k_c = 36–90 N m^{-1}) using a micromanipulator. The spring constant and sensitivity of cantilevers were calibrated prior to attaching microspheres using the JPK Nanowizard 4a. The microspheres on the AFM cantilevers were fluorinated by a 2 h chemical vapor deposition process using (1H,1H,2H,2H)-perfluorooctyl trichlorosilane (Sigma-Aldrich). To confirm the fluorination process was successful, a reference glass slide was surface treated at the same time. The base of the cantilever was moved up and down using the Z-stepper motor in the AFM head at a constant speed (approaching speed: 2 μm s^{-1}, receding speed: 0.3 μm s^{-1}, unless otherwise stated). The maximum distance for measuring the capillary force in our AFM is 15 μm. The cantilever was held stationary for 5 seconds after the particle touched the interface to allow for proper wetting of the particle. The force–distance curves were obtained during the experiment. Necessary data processing was performed in JPK SPM data processing software.

Confocal microscopy. The approaching and retraction of particles were visualized using an inverted confocal microscope (Leica SP8) with piezo-driven objectives. To observe the unmodified particle case, we used a 40× air objective with a correction ring. The correction ring was used to minimize aberrations. For the fluorinated case, the capillary bridge and meniscus are less pronounced, making it difficult to observe the contact angles using the 40× objective. For the fluorinated particles, we used a 63× oil objective to properly visualize the angles. Our 63× objective does not have a correction ring; thus, although not ideal, the aberration was corrected manually by adjusting the aspect ratio of the images using ImageJ.[81] Thickness measurements on test samples were taken to determine this correction

ratio. We utilized a laser source with a 488 nm wavelength to excite the 5(6)-carboxyfluorescein and Nile Red dyes. While the experiment was being conducted, two high-sensitivity detectors (HyD) were employed to detect the emission wavelengths of the dyes. These detectors collected emission wavelength ranges of 500–530 nm and 620–650 nm. The confocal images and videos are taken in 'xzt-plane', which allows us to take xz-images of cross-section over time. The cross-sectional images (xzt-plane) of particle interaction with the interface were taken at a resolution of 512 × 256. The entire setup allowed for the entire experiment to be recorded at a rate of ∼2 images per s.

Interfacial tension. We measured the interfacial tension of a glycerol–oil interface using the pendant drop method. A needle with an inner diameter of ∼1 mm was used to inject glycerol into silicone oil (Fig. S3, ESI†). The pendant drop images were analyzed using OpenDrop to determine the interfacial tension.[82,83]

Image analysis. The grayscale images obtained from confocal microscopy were processed using MATLAB by converting them to binarized images. The noisy background pixels were removed while preserving the shape of the wetting ridges. The glycerol–oil interface was detected along with its points of contact with the microsphere. Using these points of contact, the angles θ, β and α were then measured using ImageJ.

Roughness measurement. Surface roughness was measured by tapping mode using a JPK Nanowizard 4a atomic force microscope. To make probes stationary, fast-curing epoxy glue was spin-coated on a glass substrate. The glass microspheres were then sprinkled on the epoxy film and left to rest for 2 hours. Afterward, sharp-tip cantilevers (HQ:NSC36/Al BS, MikroMasch,) were used to scan 1 μm^2 in a dry condition. The cantilever was calibrated prior to the measurements. Subsequently, the root mean square (RMS) and peak-to-valley roughness were measured using JPK Data Processing software. Three random spots were scanned on the microspheres.

Conflicts of interest

There are no conflicts to declare.

Acknowledgements

References

1 R. Van Hooghten, V. E. Blair, A. Vananroye, A. B. Schofield, J. Vermant and J. H. Thijssen, *Langmuir*, 2017, **33**, 4107–4118.

2 D. G. Ortiz, C. Pochat-Bohatier, J. Cambedouzou, M. Bechelany and P. Miele, *Engineering*, 2020, **6**, 468–482.

3 T. Lu, H. Gou, H. Rao and G. Zhao, *J. Environ. Chem. Eng.*, 2021, **9**, 105941.

4 X. Fan, J. Yang, X. J. Loh and Z. Li, *Macromol. Rapid Commun.*, 2019, **40**, 1800203.

5 S. Xie, S. Chen, Q. Zhu, X. Li, D. Wang, S. Shen, M. Jin, G. Zhou, Y. Zhu and L. Shui, *ACS Appl. Mater. Interfaces*, 2020, **12**, 26374–26383.

6 J. H. Schröder, M. Doroshenko, D. Pirner, M. E. Mauer, B. Förster, V. Boyko, B. Reck, K. J. Roschmann, A. H. Müller and S. Förster, *Polymer*, 2016, **106**, 208–217.

7 Y. Lan, J. Choi, H. Li, Y. Jia, R. Huang, K. J. Stebe and D. Lee, *Ind. Eng. Chem. Res.*, 2019, **58**, 20961–20968.

8 W. Fei, Y. Gu and K. J. Bishop, *Curr. Opin. Colloid Interface Sci.*, 2017, **32**, 57–68.

9 E. Guzmán, F. Martínez-Pedrero, C. Calero, A. Maestro, F. Ortega and R. G. Rubio, *Adv. Colloid Interface Sci.*, 2022, 102620.

10 L. Isa, K. Kumar, M. Muller, J. Grolig, M. Textor and E. Reimhult, *ACS Nano*, 2010, **4**, 5665–5670.

11 N. Ballard, A. D. Law and S. A. Bon, *Soft Matter*, 2019, **15**, 1186–1199.

12 Y. Brasse, V. Gupta, H. T. Schollbach, M. Karg, T. A. König and A. Fery, *Adv. Mater. Interfaces*, 2020, **7**, 1901678.

13 K. Jayaprakash, U. Banerjee and A. Sen, *J. Colloid Interface Sci.*, 2017, **493**, 317–326.

14 L. Keal, C. E. Colosqui, R. H. Tromp and C. Monteux, *Phys. Rev. Lett.*, 2018, **120**, 208003.

15 T. Yin, D. Shin, J. Frechette, C. E. Colosqui and G. Drazer, *Phys. Rev. Lett.*, 2018, **121**, 238002.

16 E. Koos and N. Willenbacher, *Science*, 2011, **331**, 897–900.

17 S. Bindgen, J. Allard and E. Koos, *Curr. Opin. Colloid Interface Sci.*, 2022, **58**, 101557.

18 F. Bossler and E. Koos, *Langmuir*, 2016, **32**, 1489–1501.

19 B. S. Murray, *Adv. Colloid Interface Sci.*, 2019, **271**, 101990.

20 Z. Liu, D. J. McClements, A. Shi, L. Zhi, Y. Tian, B. Jiao, H. Liu and Q. Wang, *Crit. Rev. Food Sci. Nutr.*, 2022, 1–12.

21 E. Dickinson, *Curr. Opin. Colloid Interface Sci.*, 2010, **15**, 40–49.

22 S. Peito, D. Peixoto, I. Ferreira-Faria, A. M. Martins, H. M. Ribeiro, F. Veiga, J. Marto and A. C. Santos, *Int. J. Pharm.*, 2022, 121455.

23 A. Sarkar and E. Dickinson, *Curr. Opin. Colloid Interface Sci.*, 2020, **49**, 69–81.

24 Y. Kazemzadeh, S. E. Eshraghi, K. Kazemi, S. Sourani, M. Mehrabi and Y. Ahmadi, *Ind. Eng. Chem. Res.*, 2015, **54**, 233–239.

25 I. Nowrouzi, A. K. Manshad and A. H. Mohammadi, *J. Mol. Liq.*, 2019, **292**, 111348.

26 N. Pan, *Appl. Phys. Rev.*, 2014, **1**, 021302.

27 N. Vogel, M. Retsch, C.-A. Fustin, A. Del Campo and U. Jonas, *Chem. Rev.*, 2015, **115**, 6265–6311.

28 A. Spatafora-Salazar, D. M. Lobmeyer, L. H. Cunha, K. Joshi and S. L. Biswal, *Soft Matter*, 2021, **17**, 1120–1155.

29 J. Aizenberg, J. C. Weaver, M. S. Thanawala, V. C. Sundar, D. E. Morse and P. Fratzl, *Science*, 2005, **309**, 275–278.

30 E. Koos, J. Johannsmeier, L. Schwebler and N. Willenbacher, *Soft Matter*, 2012, **8**, 6620–6628.

31 T. Domenech and S. S. Velankar, *Soft Matter*, 2015, **11**, 1500–1516.

32 S. Bindgen, F. Bossler, J. Allard and E. Koos, *Soft Matter*, 2020, **16**, 8380–8393.

33 K. E. Jensen, R. Sarfati, R. W. Style, R. Boltyanskiy, A. Chakrabarti, M. K. Chaudhury and E. R. Dufresne, *Proc. Natl. Acad. Sci. U. S. A.*, 2015, **112**, 14490–14494.

34 Z. Cai, A. Skabeev, S. Morozova and J. T. Pham, *Commun. Mater.*, 2021, **2**, 21.

35 L. Hauer, Z. Cai, A. Skabeev, D. Vollmer and J. T. Pham, *Phys. Rev. Lett.*, 2023, **130**, 058205.

36 A. Scheludko and D. Nikolov, *Colloid Polym. Sci.*, 1975, **253**, 396–403.

37 A. Scheludko, B. Toshev and D. Bojadjiev, *J. Chem. Soc., Faraday Trans. 1*, 1976, **72**, 2815–2828.

38 M. Zanini and L. Isa, *J. Phys.: Condens. Matter*, 2016, **28**, 313002.

39 N. Vogel, J. Ally, K. Bley, M. Kappl, K. Landfester and C. K. Weiss, *Nanoscale*, 2014, **6**, 6879–6885.

40 N. Arai, S. Watanabe, M. T. Miyahara, R. Yamamoto, U. Hampel and G. Lecrivain, *Soft Matter*, 2020, **16**, 695–702.

41 V. N. Paunov, *Langmuir*, 2003, **19**, 7970–7976.

42 L. Isa, F. Lucas, R. Wepf and E. Reimhult, *Nat. Commun.*, 2011, **2**, 438.

43 C. Shi, L. Xie, L. Zhang, X. Lu and H. Zeng, *J. Colloid Interface Sci.*, 2020, **558**, 173–181.

44 J. Bowen, D. Cheneler, J. W. Andrews, A. R. Avery, Z. Zhang, M. C. Ward and M. J. Adams, *Langmuir*, 2011, **27**, 11489–11500.

45 D. Yang, X. Peng, Q. Peng, T. Wang, C. Qiao, Z. Zhao, L. Gong, Y. Liu, H. Zhang and H. Zeng, *Engineering*, 2022, **18**, 49–61.

46 L. Xie, J. Wang, Q. Lu, W. Hu, D. Yang, C. Qiao, X. Peng, Q. Peng, T. Wang and W. Sun, *Adv. Colloid Interface Sci.*, 2021, **295**, 102491.

47 L. Xie, X. Cui, L. Gong, J. Chen and H. Zeng, *Langmuir*, 2020, **36**, 2985–3003.

48 M. Pan, L. Gong, L. Xiang, W. Yang, W. Wang, L. Zhang, W. Hu, L. Han and H. Zeng, *J. Membr. Sci.*, 2021, **625**, 119140.

49 X. Mao, D. Yang, L. Xie, Q. Liu, T. Tang, H. Zhang and H. Zeng, *J. Phys. Chem. B*, 2021, **125**, 7320–7331.

50 M. P. Neubauer, M. Poehlmann and A. Fery, *Adv. Colloid Interface Sci.*, 2014, **207**, 65–80.

51 N. Yang, C. Su, Y. Zhang, J. Jia, R. L. Leheny, K. Nishinari, Y. Fang and G. O. Phillips, *J. Colloid Interface Sci.*, 2020, **570**, 362–374.

52 W. A. Ducker, T. J. Senden and R. M. Pashley, *Nature*, 1991, **353**, 239–241.

53 W. A. Ducker, T. J. Senden and R. M. Pashley, *Langmuir*, 1992, **8**, 1831–1836.

54 J. K. Ferri, P. Carl, N. Gorevski, T. P. Russell, Q. Wang, A. Böker and A. Fery, *Soft Matter*, 2008, **4**, 2259–2266.

55 J. Erath, S. Schmidt and A. Fery, *Soft Matter*, 2010, **6**, 1432–1437.

56 S. M. Flores and J. L. Toca-Herrera, *Nanoscale*, 2009, **1**, 40–49.

57 A. B. Mathur, G. A. Truskey and W. M. Reichert, *Biophys. J.*, 2000, **78**, 1725–1735.

58 A. E. Brown, A. Hategan, D. Safer, Y. E. Goldman and D. E. Discher, *Biophys. J.*, 2009, **96**, 1952–1960.

59 A. Vial, C. Taveneau, L. Costa, B. Chauvin, H. Nasrallah, C. Godefroy, P. Dosset, H. Isambert, K. X. Ngo and S. Mangenot, *Nanoscale*, 2021, **13**, 12484–12493.

60 C. Poudel, I. Mela and C. F. Kaminski, *Methods Appl. Fluoresc.*, 2020, **8**, 024005.

61 N. Hain, S. Handschuh-Wang, D. Wesner, S. I. Druzhinin and H. Schönherr, *J. Colloid Interface Sci.*, 2019, **547**, 162–170.

62 T. F. Fernandes, O. Saavedra-Villanueva, E. Margeat, P.-E. Milhiet and L. Costa, *Sci. Rep.*, 2020, **10**, 7098.

63 R. F. Tabor, H. Lockie, D. Mair, R. Manica, D. Y. Chan, F. Grieser and R. R. Dagastine, *J. Phys. Chem. Lett.*, 2011, **2**, 961–965.

64 M. Eriksson, M. Tuominen, M. Jarn, P. M. Claesson, V. Wallqvist, H.-J. R. Butt, D. Vollmer, M. Kappl, J. Schoelkopf and P. A. Gane, *ACS Nano*, 2019, **13**, 2246–2252.

65 S. Mettu, Q. Ye, M. Zhou, R. Dagastine and M. Ashokkumar, *Soft Matter*, 2018, **14**, 3192–3201.

66 J. T. Pham, F. Schellenberger, M. Kappl and H.-J. Butt, *Phys. Rev. Mater.*, 2017, **1**, 015602.

67 J. D. Glover and J. T. Pham, *Soft Matter*, 2020, **16**, 5812–5818.

68 F. Schellenberger, P. Papadopoulos, M. Kappl, S. A. L. Weber, D. Vollmer and H. J. Butt, *Phys. Rev. Lett.*, 2018, **121**, 048002.

69 J. D. Glover, X. Yang, R. Long and J. T. Pham, *Nat. Commun.*, 2023, **14**, 2362.

70 S. E. Anachkov, I. Lesov, M. Zanini, P. A. Kralchevsky, N. D. Denkov and L. Isa, *Soft Matter*, 2016, **12**, 7632–7643.

71 Y. Tang and S. Cheng, *Phys. Rev. E*, 2018, **98**, 032802.

72 Q.-X. Huang, Y.-T. Fei, S. Gonda, I. Misumi, O. Sato, T. Keem and T. Kurosawa, *Meas. Sci. Technol.*, 2006, **17**, 1417–1423.

73 S. Moreno-Flores, *Microsc. Res. Tech.*, 2016, **79**, 1045–1049.

74 N. Cross and R. Picknett, *Trans. Faraday Soc.*, 1963, **59**, 846–855.

75 T. Gillespie and W. Settineri, *J. Colloid Interface Sci.*, 1967, **24**, 199–202.

76 H.-J. Butt, W. J. P. Barnes, A. Del Campo, M. Kappl and F. Schönfeld, *Soft Matter*, 2010, **6**, 5930–5936.

77 H.-J. Butt and M. Kappl, *Adv. Colloid Interface Sci.*, 2009, **146**, 48–60.

78 J. Ally, E. Vittorias, A. Amirfazli, M. Kappl, E. Bonaccurso, C. E. McNamee and H.-J. R. Butt, *Langmuir*, 2010, **26**, 11797–11803.

79 M. Zanini, I. Lesov, E. Marini, C.-P. Hsu, C. Marschelke, A. Synytska, S. E. Anachkov and L. Isa, *Langmuir*, 2018, **34**, 4861–4873.

80 A. G. Banpurkar, K. P. Nichols and F. Mugele, *Langmuir*, 2008, **24**, 10549–10551.

81 C. A. Schneider, W. S. Rasband and K. W. Eliceiri, *Nat. Methods*, 2012, **9**, 671–675.

82 J. D. Berry, M. J. Neeson, R. R. Dagastine, D. Y. Chan and R. F. Tabor, *J. Colloid Interface Sci.*, 2015, **454**, 226–237.

83 E. Huang, A. Skoufis, T. Denning, J. Qi, R. R. Dagastine, R. F. Tabor and J. D. Berry, *J. Open Source Software*, 2021, **6**, 2604.